Hierarchical crack buffering triples ductility in eutectic herringbone high-entropy alloys

Authors: Peijian Shi[1], Runguang Li[2], Yi Li[1], Yuebo Wen[1], Yunbo Zhong[1]*, Weili Ren[1], Zhe Shen[1], Tianxiang Zheng[1], Jianchao Peng[3], Xue Liang[3], Pengfei Hu[3], Na Min[3], Yong Zhang[2], Yang Ren[4], Peter K. Liaw[5], Dierk Raabe[6]* & Yan-Dong Wang[2,7]*

Affiliations:

[1]State Key Laboratory of Advanced Special Steel, Shanghai Key Laboratory of Advanced Ferrometallurgy, School of Materials Science and Engineering, Shanghai University, Shanghai, China.

[2]Beijing Advanced Innovation Center for Materials Genome Engineering, State Key Laboratory for Advanced Metals and Materials, University of Science and Technology Beijing, Beijing, China.

[3]Laboratory for Microstructures, Shanghai University, Shanghai, China.

[4]X-Ray Science Division, Advanced Photon Source, Argonne National Laboratory, Argonne, IL, USA.

[5]Department of Materials Science and Engineering, The University of Tennessee, Knoxville, TN, USA.

[6]Department Microstructure Physics and Alloy Design, Max-Planck-Institut für Eisenforschung, Düsseldorf, Germany.

[7]Key Laboratory for Anisotropy and Texture of Materials (Ministry of Education), School of Material Science and Engineering, Northeastern University, Shenyang 110819, China.

*Corresponding author. Email: yunboz@staff.shu.edu.cn; d.raabe@mpie.de; ydwang@mail.neu.edu.cn

ABSTRACT

Tolerating cracks in human-made malleable materials is counterintuitive as micro-damage usually limits material lifetime rather than enhancing it. Some composites, such as bone, have hierarchical microstructures that feature crack tolerance, but cannot withstand high elongation. We successfully reconcile crack tolerance and high elongation, demonstrated with a directionally-solidified eutectic high-entropy alloy (EHEA). The solidified alloy has a hierarchically-organized herringbone structure that equips a bionic-inspired hierarchical crack buffering. This effect guides stable, persistent, crystallographic nucleation and growth of multiple micro-cracks in abundant poor-deformability microstructures. The structure helps the cracks avoid catastrophic growth and percolation, due to a hierarchical buffering by adjacent dynamic strain-hardened features. Our self-buffering herringbone material yields an ultrahigh uniform tensile elongation (~50%), three times that of conventional non-buffering EHEAs, without sacrificing strength.

Cracks occur in materials if loads cannot be fully dissipated by elastic-plastic work, exposing human lives to risk of failure and integrity loss of safety-critical components (*1*–*6*). Some hierarchical composites, such as high-toughness bone (*3*), feature excellent crack tolerance, but they usually cannot withstand high elongations due to the lack of conventional lattice defects to bear tensile deformation (*1*–*3*). By contrast, tolerating cracks in human-engineered formable materials is counterintuitive as extensive cracks tend to trigger the premature failure (*6*). More specifically, these cracks are generally initiated from the localized severe plastic deformation, and their propagation cannot be effectively buffered and arrested (*5*–*8*). This situation is due to the fact that the locally-deformed microstructures are usually not characterized by sufficiently sustainable strain-hardening capability used to relieve locally high stresses at the propagating tips of cracks (*1*–*4*). So even though some ductile metallic composites exhibit crack tolerance, only limited additional tensile ductility can be achieved (*5*–*11*). Overall, in human-made materials the total elongation in conjunction with crack tolerance is usually not as high as we would expect (*5*–*11*). We show that the conflict between extensive crack generation and high uniform elongation can be broken in eutectic high-entropy alloys (EHEAs). EHEAs are a family of recently developed multi-principal-element lamellar composites (*12*–*15*). We demonstrate that in EHEAs a herringbone-like hierarchical eutectic microstructure design tends to generate a high density of cracks upon tensile deformation. However, the hierarchical crack buffering prevents them from growing and percolating catastrophically across a huge straining range of ~25%. Consequently, such a high density of cracks is not detrimental to the elongation, but instead can serve as an effective strategy to compensate for the limited tensile ductility of the poor-deformability lamellae. This renders ultrahigh isostrain forming conditions among adjacent lamellae with different deformability, thus achieving a surprisingly high uniform elongation of ~50%. This value is three times that of conventional EHEAs without this type of crack tolerance.

We studied two as-cast $Al_{19}Fe_{20}Co_{20}Ni_{41}$ (at.%) EHEAs (*15*) fabricated by conventional casting and directional solidification (DS), respectively. The conventionally-cast EHEA served as the reference material and exhibited a typical lamellar microstructure (Fig. 1A) formed during a eutectic transformation (*14*). The structure is comprised of $L1_2$ (soft ordered face-centered-cubic) and B2 (hard ordered body-centered-cubic) dual-phase lamellae with varying growth directions in different near-equiaxed grains (Fig. 1B, C). The directionally-solidified EHEA displays a directionally-grown microstructure (Fig. 1D). It consists of columnar grains aligned along the DS direction (Fig. 1E). They contain aligned (grain center) and branched (rims of the grains) eutectic colonies, both of which comprise soft $L1_2$ and hard B2 lamellae with nano-indentation hardness of ~4.2 GPa and ~5.6 GPa, respectively (Fig. 1E). Lamellae consisting of aligned eutectic colonies (AEC, accounting for ~33 vol.%) generally grow along the DS direction, whereas lamellae comprising branched eutectic colonies (BEC, 67 vol.%) are inclined at 30~60 degrees to the DS direction, and have a more branched morphology. With these features the directionally-solidified EHEA assumes a new type of hierarchically-arranged herringbone microstructure (Fig. 1F). We show that this bone-like structure is formed by the directional growth of cellular solid-liquid interfaces along the DS direction (*16–21*). The lamellae of both colonies grow perpendicular to the cellular interfaces (Fig. 1I and fig. S1). We did not detect any precipitates or other phases in the dual-phase lamellae by selected-area-electron diffraction patterns and high-resolution high-angle annular dark-field scanning transmission-electron microscopy (HAADF-STEM, Fig. 1G and fig. S1). We confirmed this observation with synchrotron high-energy X-ray diffraction (SHE-XRD, Fig. 1H). Our HAADF-STEM energy-dispersive spectroscopy analysis shows that the DS process has a negligible effect on the chemical composition distribution of the eutectic lamellae (fig. S2). We also obtained three-dimensional stereographic microstructure images of the two as-cast EHEAs (fig. S3). The average width of the columnar grains and its $L1_2$-phase content are ~54 μm and ~59 vol.% in the directionally-solidified EHEA, respectively. Both values are slightly larger than in the conventionally-cast reference EHEA (grain size ~48 μm and $L1_2$-phase content ~55 vol.%). These two discrepancies are due to the slower cooling rate of the molten EHEA during DS compared to the condition that during transient solidification when preparing the reference EHEA. The eutectic lamellar spacing of the reference EHEA is ~2.1 μm, which is smaller than that of the AEC (~2.8 μm) and the BEC (mainly varying in the range 3~8 μm). Variable lamellar spacing in the BEC results in significant hardness fluctuations (192~247 HV) compared to the AEC (263 ± 10 HV).

We observed a remarkable ductility improvement, quantified from engineering stress-strain curves (Fig. 2A), of the directionally-solidified compared to the conventionally-cast reference material. The uniform elongation tripled, increasing from ~16% for the reference EHEA to ~50% for the directionally-solidified EHEA. Additionally, the directionally-solidified EHEA has a ~150-MPa higher yield strength than the conventionally-cast EHEA. Although the directionally-solidified EHEA has a high content of hard, low-ductility B2 phase (~41 vol.%) (*15*, *22*, *23*), it nonetheless exhibits a large uniform elongation of ~50%. Its elongation is comparable to that of widely-studied, high-ductility, and fully homogenized face-centered-cubic high-entropy alloys (HEAs) (*24*–*27*). The resulting strength–ductility combination, and especially the uniform ductility, in the directionally-solidified EHEA outperforms that of any other as-cast eutectic and near-eutectic HEAs (*14*, *15*, *19*, *20*, *22*, *23*, *28*–*33*) (Fig. 2B).

We attribute the gain in ductility of the directionally-solidified material to its hierarchical herringbone microstructure and the effect that this structure has on crack buffering, as we revealed with detailed characterizations of the deformation and fracture mechanisms (Fig. 3). The post-fractured specimen surface of the EHEA, which we characterized by scanning-electron microscopy (SEM), shows a large number of micro-cracks (Fig. 3H). The micro-crack density is as large as ~8×10^4 mm^{-2} in the AEC, and the micro-crack spacing is as small as ~0.83 μm in some B2 lamellae of the AEC. We do not find the otherwise typical large secondary cracks that are observed in conventional as-cast materials (*5*) (fig. S5). The micro-cracks we observed are mainly distributed in the hard B2 lamellae of the AEC (Fig. 3H), yet they seem to have ultrahigh stability. The cracks remain strictly confined in the individual B2 phase where they formed, and no crack percolation into neighboring B2 lamellae occurs. This applies even in B2 regions with multiple micro-cracks that are separated by only a single $L1_2$ lamella

(Fig. 3H). Interestingly, we detected high micro-crack populations already at early and medium strains of up to ~25% (Fig. 3J). Considering the ~50% total ductility, the material features a capability to withstand ~25% more straining after the onset of the first massive crack initiation at modest strains. In this deformation regime, no crack percolation or catastrophic failure event occur irrespective of the extreme abundance of micro-cracks (Fig. 3E–H). This observation substantiates our claim that this alloy has extreme crack tolerance and a crack-mediated ductility reserve of ~25%.

To further verify the exceptional crack tolerance, we evaluated the fracture resistance of the directionally-solidified herringbone EHEA by measuring *J*-integral–based *R*-curves—*J* as a function of the stable crack extension, Δa—using single-edge bend specimens in accordance with the ASTM Standard E1820 (*34*). The crack-resistance (*R*-curve) behavior (fig. S6A) displays a surprisingly high crack-initiation fracture toughness J_{Ic}, determined essentially at $\Delta a \rightarrow 0$, of ~318 kJ/m^2, and a crack-growth toughness J_{ss} of ~430 kJ/m^2 at a valid crack extension Δa of ~1 mm. These toughness values are over 2 times higher than those in the conventionally-cast EHEA (fig. S6A). These fracture properties are comparable with those of high-toughness gradient-structured materials reported recently (*35*). Thus, these trends demonstrate extreme crack resistance and damage tolerance of the herringbone EHEA.

To illuminate the underlying mechanisms responsible for the extraordinary crack tolerance, we characterized the dynamic micro-crack evolution in the directionally-solidified herringbone structure (Fig. 3E–H). We revealed an in-situ developing hierarchical interplay between crystallographic micro-crack guidance and crack blunting. We first observed the evolution of dense slip lines on the pre-polished surface of the hard B2 lamellae (Fig. 3E). These slip lines mark regions of strong linear strain localization, stemming from prevalent activation of the primary slip system with highest Schmid factor (*35*–*38*). This promotes formation of micro-cracks in the B2 lamellae and their linear crystallographic propagation along these slip lines (Fig. 3E, F). Quantitative analysis of these micro-cracks reveals a rapid increase in crack density in this strain stage (Stage I in Fig. 3J), which subsequently increases modestly towards near-saturation. This behavior differs from the gradually-increasing crack density observed in most common materials (*10*). Surprisingly, this rapid increase in micro-crack population occurs in a relatively-small intermediate strain range of 25~30%. The resulting micro-crack density is up to $\sim 5.5 \times 10^4$ mm^{-2}, which is over twice the density increase found in the subsequent large strain range of 30~50% (Fig. 3J). Interestingly, these multiple cracks do not cause specimen rupture, thus revealing an impressive tolerance of the plastically-deformed material against percolative crack expansion and catastrophic failure.

We observed that the micro-cracks emerging in the B2 phase got arrested at the interfaces to the alternatingly adjacent $L1_2$ lamellae of the AEC (Fig. 3F). These softer $L1_2$ lamellae serve as soft crack buffers, that act on the tips of micro-cracks, blunt them, and shield the associated high local stresses (*10, 35, 39*). Without the presence of such alternating soft buffer layers, the cracks would have percolated forward. When the micro-cracks have penetrated an entire B2-lamellar cross section, the neighboring soft

$L1_2$ lamellae blunt the crack tips, as evidenced by their rounded shapes (*10*) (Fig. 3G). Also, for triggering sample fracture, micro-cracks would not only have to cut through the $L1_2$ lamellae and thus cut the whole AEC, but also penetrate into the adjacent BEC zone. This means that the herringbone microstructure has two hierarchical levels that feature crack arresting properties, namely, the alternating hard-soft (B2-$L1_2$) phase layers and the changing alignment of the eutectic colonies. Further three-point bending experiments reveal that this hierarchical effect effectively blunts the crack tip and buffers the crack propagation (fig. S8) (*21*), thus rendering the directionally-solidified herringbone EHEA with concurrently excellent fracture toughness (fig. S6A) (*39*).

Another important effect is that during tension new micro-cracks are frequently generated in the free intact material portions between these fully-extended cracks within every single B2 lamella (Fig. 3G, H). This crack pattern refinement releases stress concentrations around phase interfaces and weakens the stress intensity at the tips of larger micro-cracks (*1*–*6*).

Thus, further growth of these fully-extended micro-cracks requires increased mechanical loads for developing them into unstable and critical larger cracks that can cause failure (*1*–*3*). However, the overall directional topology of the phases and interfaces means that these micro-cracks can only grow with an alignment towards the tensile (and not transverse) direction in the B2 lamellae of the AEC. Numerous micro-cracks develop in such a fashion assuming stable parallelogram-like shapes (Fig. 3H). We confirmed these experimental observations with high-resolution focused-ion-beam imaging (fig. S5C) and quantitative micro-crack studies (Stage III in Fig. 3J). This stage features a very slow increase in micro-crack density and length. But these micro-cracks in the low-ductility B2 lamellae of the AEC exhibit a surprisingly high capacity to accommodate their shapes and thus carry strains, as revealed by their parallelogram-like morphology (Fig. 3H). Even in this high load regime no interface delamination cracks are found in the herringbone structure. This effect is attributed to their semi-coherent interface structure that can bear high shear stresses (*17*) (fig. S9).

By contrast, in the absence of crack tolerance, early failure occurs in the conventionally-cast EHEA. In the directionally-solidified material, the strain tolerated by the hierarchical herringbone structure, with its high density of cracks in the 25~50% tensile strain regime, exceeds the overall elongation (~16%, Fig. 2A) of the conventionally-cast EHEA. In general, the cumulative crack damage of the material's cross section will gradually reduce its effective load-bearing capability per unit area, thus decreasing the apparent nominal tensile stress (*6–11*). However, this trend does not appear in the directionally-solidified material (Fig. 2A), despite its high crack density.

We investigated the microstructure in detail at the nanoscale to better understand the crack-tolerance mechanisms. Aberration-corrected transmission-electron microscopy (TEM, Fig. 4) shows that the directional movement of massive dislocations in the crystal interior produces the pronounced crystallographic slip-line structures (*35–38*), also visible on the pre-polished sample surfaces (Fig. 3). The deformation of the B2 lamellae is dominated by planar slip of screw dislocations on {110}<111> slip systems, and the

$L1_2$ lamellae show planar-dislocation slip on {111}<011> (Fig. 4A, B and fig. S10). As deformation proceeds, the B2 lamellae undergo increasing planar-dislocation shear (characterized by dramatically-reduced dislocation spacing at tensile strains of 10~25%, fig. S11H). This leads to a gradual exhaustion of deformability (fig. S11E–H). The exhausted node corresponds roughly to ~25% tensile strain, thus triggering extensive micro-crack initiation at the low strain range of 25~30% (Fig. 3E, J) and their crystallographic propagation along these slip lines inside the B2 lamellae (Fig. 3F, G). In the $L1_2$ lamellae, however, we found a dynamic substructure refinement governed by sequentially-activated multi-slip dislocation shear and microband formation (Fig. 4). At a tensile strain of ~5%, the deformation of the $L1_2$ lamellae is at first dominated by planar-dislocation slip evolving into a banded shear morphology (Fig. 4A). In these slip bands, the spacing among adjacent dislocations gradually decreases from the lamellar interior towards the lamellar interfaces (fig. S11A), thereby establishing a long-range strain gradient (*40, 41)*. These dislocations, piled up against the interfaces, are known as geometrically-necessary dislocations (GNDs), creating back-stress hardening (*40*). At ~15% strain, these pronounced planar dislocations evolve into well-developed slip bands (*42*) (Fig. 4D). Subsequently, we observed deformation-driven refinement of slip bands. Fresh slip bands are constantly generated in the free space between initially-existing ones (Fig. 4E). The increasing slip-band density supports substantial dislocation storage, accompanied by back-stress hardening. By conducting loading-unloading-reloading experiments, we detected a back stress-dominated high kinematic strengthening effect (holding about two-thirds of the applied stress, fig. S12) (*40*, *43*).

This quantitatively confirms the leading role of back-stress hardening in the $L1_2$ lamellae at this stage. Upon further straining we observed dislocations in wavy-slip patterns between slip bands (Fig. 4E). This suggests that dislocation cross-slip is activated, inducing forest dislocation hardening (*43*) (fig. S12). At higher strains of 35~42%, we observed deformation-induced microbands that subdivide the $L1_2$ lamellae into numerous plate-like misoriented domains (*43–45*) (Fig. 4C, F). Thus, these microbands, analogous to low-angle grain boundaries (not twins, evidenced by Fig. 4F, inset), are associated with further lamellar subdivision and refinement. This mechanism promotes a microband-induced hardening effect, as demonstrated by the surprisingly high strain-hardening rate (Fig. 2A, inset).

As we further discovered using low-angle annular dark-field STEM (fig. S13), this dynamic substructure refinement favors substantial local strain hardening in the vicinity of the incoming crack tips (*3*), thus turning the $L1_2$ lamellae into very efficient crack buffer regions. This phenomenon endows the herringbone structure with excellent crack tolerance (Fig. 3K). Besides the plastic buffering and crack blunting effect, strong strain hardening of the $L1_2$ lamellae (Fig. 4C–F) contributes to the high load-bearing capability of the material. This counteracts the potential softening effect caused by micro-cracks in the B2 phase, as revealed by the fact that the material does not lose but gain tensile strength (Fig. 2A). To provide quantitative insights into the exceptional load-bearing capability, we performed in-situ synchrotron experiments. We observed a real-time stress partitioning effect (*46–48*) between the B2 and $L1_2$ phases, based on the SHE-XRD results (Fig. 4G). As we expected, the yielding of the $L1_2$ phase leads to stress relaxation and stress transfer to the hard B2 phase. This trend is known from other dual-phase composites (*46–48*). Stress partitioning to hard phases usually increases continuously until fracture (*46*). However, in the herringbone structure the B2 phase bears decreasing stress after reaching a tensile strain of ~25%, whereas the $L1_2$ phase exhibits an opposite trend with remarkable strain-hardening behavior (Fig. 4G). This marks a gradual transfer of the load from the hard but brittle B2 phase to the initially soft but gradually strain-hardened $L1_2$ phase. This means that the SHE-XRD probing elucidates that the load-bearing capacity of the $L1_2$ phase increases substantially due to dynamic substructure refinement, while that of the B2 phase decreases gradually caused by increasing internal micro-cracking. To compensate the limited TEM-sampling area, we also conducted 2D SHE-XRD diffraction investigations (*48*), covering the entire 360°-azimuthal range recorded for different planes near the point of fracture (Fig. 4H). No new diffraction lines are detected, suggesting that the high load-bearing capability of the herringbone structure is not caused by conventional phase transformation. However, the diffraction lines of the B2 phase (e.g., marked by red lines) deviate severely from their initial angle. This is caused by the huge elastic strain of the B2 phase (up to ~5.5%, fig. S14). This observation is also revealed by the conventionally-cast EHEA, which shows delayed dislocation shear in the B2 lamellae (fig. S15).

When further exploring the hierarchical herringbone structure and its microstructural evolution during tensile deformation, we identified a slip-line-mediated sequential deformation transfer from the soft BEC to the hard AEC (Fig. 3A–D) (*21*). This finding reveals that the BEC features high deformability that allows compatible deformation of adjacent columnar grains (Fig. 3D). At the early deformation stage, dense dislocation pile-up arrays against phase interfaces were observed in the $L1_2$ lamellae of the BEC (Figs. 3A, 4A). The associated pile-up stresses are accommodated by the elastic deformation of the plastically-less compliant B2 lamellae (Fig. 3B), thereby shielding high stress concentrations (*48*), a mechanism which supports compatible co-deformation of adjacent phases and colonies (*49*). The large local misorientation shown in the kernel average misorientation (KAM) map (Fig. 3I) confirms that the plastic strain incompatibility can be well accommodated in the BEC. As the deformation progresses, stable micro-cracks, as observed in the AEC, can also be generated in the low-ductility B2 lamellae of the BEC, assisting its compliance (fig. S16). These mechanisms of mechanical energy release in the adjacent phases and colonies reduce the chance of grain-boundary decohesion or cracking (*40, 49*) (fig. S5B), unlike accessible in conventionally cast EHEA. The statistically-distributed lamellar arrangements in the differently-oriented grains cannot sustain a compatible co-deformation among them (*21*). Consequently, grain-boundary cracking concomitant with mechanical instability triggers premature failure (i.e., deteriorating tensile ductility) (fig. S17–19) and also limits the fracture toughness level of the conventionally-cast material (*40, 49*) (figs. S6, 7).

Natural materials with high toughness often also comprise hard and soft components in hierarchical layered architectures (*50–52*). The lamellar cortical bone, a prime example, consists of mineralized collagen fibrils and a non-fibrillar organic matrix, which acts as a 'glue' that holds the mineralized fibrils together (*50–52*). Healthy lamellar bone resists fracture through complementary intrinsic and extrinsic contributions throughout its hierarchical structure (*50, 52*). The glue-mediated fibrillar sliding mechanism, analogous to the dislocation-assisted inelastic deformation in our herringbone EHEA, is essential to promote high plasticity (*50*). In both materials, plasticity and the resultant ductility provide a major contribution to the intrinsic toughness by dissipating energy and forming plastic zones surrounding incipient cracks, which further serves to blunt crack tips, thereby reducing the driving force for cracking (*3, 50*). The extrinsic mechanisms, such as collagen-fibre bridging and crack deflection, act principally on the wake of cracks to reduce (shield) the local stresses/strains experienced at crack tips and inhibit their propagation (*50*). These effects exhibit a marked similarity to what we identified in our herringbone material (see Fig. 3E–H and fig. S8). Of course, a salient characteristic of bone is its ability to remodel itself to heal and repair damage—a trait that is difficult to replicate in our synthetic materials (*50, 51*).

In summary, we presented a hierarchical microstructure design approach, realized in a directionally-solidified bulk EHEA, that allows reconciliation of crack tolerance and high uniform elongation, features that are usually mutually exclusive in both, human-made and biological materials. The crack tolerance is maintained over a huge range of ~25% tensile elongation and enables to triple the ductility of the material by a factor of 3 relative to conventionally solidified material, without sacrificing strength. These proposed mechanisms exhibit practical merits in guiding a broader group of eutectic-type cast HEA and traditional alloy development. The microstructure approach can be potentially realized also in other bulk materials consisting of hard and soft phases that can be rendered into hierarchically organized herringbone microstructures, enabling the design of crack-tolerant yet high-deformability materials not by avoiding cracks but by guiding and buffering them. Furthermore, this hierarchical herringbone microstructure design approach and the salient effect it has on crack buffering show a promising guidance in designing not only new hierarchically-structured alloys with high elongation but also new bone substituting biomaterials with excellent fracture toughness.

References

1. R. O. Ritchie, The conflicts between strength and toughness. *Nat. Mater.* **10**, 817−822 (2011).
2. H. J. Gao, B. H. Ji, I. L. Jäger, E. Arzt, P. Fratzl, Materials become insensitive to flaws at nanoscale: lessons from nature. *P. Natl. Acad. Sci. USA* **100**, 5597−5600 (2003).
3. M. Koyama *et al.*, Bone-like crack resistance in hierarchical metastable nanolaminate steels. *Science* **355**, 1055−1057 (2017).
4. L. Liu *et al.*, Making ultrastrong steel tough by grain-boundary delamination. *Science* **368**, 1347−1352 (2020).
5. P. J. Shi *et al.*, Enhanced strength–ductility synergy in ultrafine-grained eutectic high-entropy alloys by inheriting microstructural lamellae. *Nat. Commun.* **10**, 489 (2019).
6. B. H. Sun *et al.*, Revealing fracture mechanisms of medium manganese steels with and without delta-ferrite. *Acta Mater.* **164**, 683–696 (2019).
7. D. Y. Yan, C. C. Tasan, D. Raabe, High resolution in situ mapping of microstrain and microstructure evolution reveals damage resistance criteria in dual phase steels. *Acta Mater.* **96**, 399–409 (2015).
8. A. Alaie, J. Kadkhodapour, S. Z. Rad, M. A. Asadabad, S. Schmauder, Formation and coalescence of strain localized regions in ferrite phase of DP600 steels under uniaxial tensile deformation. *Mater. Sci. Eng. A* **623**, 133−144 (2015).

9. M. Koyama, C. C. Tasan, E. Akiyama, K. Tsuzaki, D. Raabe, Hydrogen-assisted decohesion and localized plasticity in dual-phase steel. *Acta Mater*. **70**, 174−187 (2014).

10. M. M. Wang, C. C. Tasan, D. Ponge, A. C. Dippelb, D. Raabe, Nanolaminate transformation-induced plasticity–twinning-induced plasticity steel with dynamic strain partitioning and enhanced damage resistance. *Acta Mater*. **85**, 216–228 (2015).

11. Z. Li *et al.*, Enhanced mechanical properties of graphene (reduced graphene oxide)/aluminum composites with a bioinspired nanolaminated structure. *Nano Lett.* **15**, 8077−8083 (2015).

12. J. W. Yeh *et al.*, Nanostructured high-entropy alloys with multiple principal elements: novel alloy design concepts and outcomes. *Adv. Eng. Mater.* **6**, 299−303 (2004).

13. E. P. George, D. Raabe, R. O. Ritchie, High-entropy alloys. *Nat. Rev. Mater*. **4**, 515−534 (2019).

14. Y. P. Lu *et al.*, A promising new class of high-temperature alloys: eutectic high-entropy alloys. *Sci. Rep.* **4**, 6200 (2014).

15. X. Jin, Y. Zhou, L. Zhang, X. Y. Du, B. S. Li, A novel $Fe_{20}Co_{20}Ni_{41}Al_{19}$ eutectic high entropy alloy with excellent tensile properties. *Mater. Lett.* **216**, 144−146 (2018).

16. Z. Shang *et al.*, Investigations on the microstructure and room temperature fracture toughness of directionally solidified NiAl–Cr(Mo) eutectic alloy. *Intermetallics* **57**, 25−33 (2015).

17. H. Bei, E. P. George, Microstructures and mechanical properties of a directionally solidified NiAl–Mo eutectic alloy. *Acta Mater.* **53**, 69−77 (2005).

18. Z. Shang, J. Shen, G. Liu, Y. H. Xu, Microstructure evolution of directionally solidified NiAl–28Cr–6Mo eutectic alloy under different withdrawal rates. *Mater. Sci. Tech-Lond.* **34**, 1839−1846 (2018).

19. H. T. Zheng *et al.*, Phase separation of $AlCoCrFeNi_{2.1}$ eutectic high-entropy alloy during directional solidification and their effect on tensile properties. *Intermetallics* **113**, 106569 (2019).

20. L. Wang *et al.*, Microstructures and room temperature tensile properties of as-cast and directionally solidified $AlCoCrFeNi_{2.1}$ eutectic high-entropy alloy. *Intermetallics* **118**, 106681 (2020).

21. Materials and Methods are available as Supplementary Materials on Science Online.

22. H. Jiang *et al.*, Tensile deformation behavior and mechanical properties of a bulk cast $Al_{0.9}CoFeNi_2$ eutectic high-entropy alloy. *J. Mater. Sci. Technol.* **61**, 119−124 (2021).

23. Y. P. Lu *et al.*, Directly cast bulk eutectic and near-eutectic high entropy alloys with balanced strength and ductility in a wide temperature range. *Acta Mater.* **124**, 143−150 (2017).

24. B. Gludovatz *et al.*, A fracture-resistant high-entropy alloy for cryogenic applications. *Science* **345**, 1153−1158 (2014).

25. W. Q. Guo *et al.*, Dislocation-induced breakthrough of strength and ductility trade-off in a non-equiatomic high-entropy alloy. *Acta Mater.* **185**, 45−54 (2020).

26. Y. H. Jo *et al.*, Cryogenic strength improvement by utilizing room-temperature deformation twinning in a partially recrystallized VCrMnFeCoNi high-entropy alloy. *Nat. commun.* **8**, 15719 (2017).
27. Q. Y. Lin *et al.*, Cryogenic-deformation-induced phase transformation in an FeCoCrNi high-entropy alloy. *Mater. Res. Lett.* **6**, 236−243 (2018).
28. X. Jin, Y. Zhou, L. Zhang, X. Y. Du, B. S. Li, A new pseudo binary strategy to design eutectic high entropy alloys using mixing enthalpy and valence electron concentration. *Mater. Design* **143**, 49−55 (2018).
29. Z. S. Yang *et al.*, Enhancing the mechanical properties of casting eutectic high entropy alloys with Mo addition. *Appl. Phys. A* **125**, 208 (2019).
30. L. L. Ma, J. N. Wang, P. P. Jin, Microstructure and mechanical properties variation with Ni content in $Al_{0.8}CoCr_{0.6}Fe_{0.7}Ni_x$ (x = 1.1, 1.5, 1.8, 2.0) eutectic high-entropy alloy system. *Mater. Res. Exp.* **7**, 016566 (2020).
31. X. Jin *et al.*, A new $CrFeNi_2Al$ eutectic high entropy alloy system with excellent mechanical properties. *J. Alloy. Compd.* **770**, 655−661 (2019).
32. Q. F. Wu *et al.*, Uncovering the eutectics design by machine learning in the Al-Co-Cr-Fe-Ni high entropy system. *Acta Mater.* **182**, 278−286 (2020).
33. X. Jin, Y. X. Liang, J. Bi, B. S. Li, Enhanced strength and ductility of $Al_{0.9}CoCrNi_{2.1}$ eutectic high entropy alloy by thermomechanical processing. *Materialia.* **10**, 100639 (2020).
34. E08 Committee, E1820 Standard Test Method for Measurement of Fracture Toughness (ASTM International, 2017).

35. R. Q. Cao *et al.*, On the exceptional damage-tolerance of gradient metallic materials. *Mater. Today* **32**, 94–107 (2020).

36. S. L. Wei *et al.*, Natural-mixing guided design of refractory high-entropy alloys with as-cast tensile ductility. *Nat. Mater.* **19,** 1175–1181 (2020).

37. S. Mader, A. Seeger, C. Leitz, Work hardening and dislocation arrangement of FCC single crystals. I. Plastic deformation and slip line studies of nickel single crystals. *J. Appl. Phys.* **34**, 3368−3375 (1963).

38. Z. F. Lei *et al.*, Enhanced strength and ductility in a high-entropy alloy via ordered oxygen complexes. *Nature* **536**, 546−550 (2018).

39. Z. J. Zhang *et al.*, Nanoscale origins of the damage tolerance of the high-entropy alloy CrMnFeCoNi. *Nat. Commun.* **6**, 10143 (2015).

40. Y. T. Zhu *et al.*, Heterostructured materials: superior properties from hetero-zone interaction. *Mater. Res. Lett.* **9**, 1−31 (2021).

41. E. Ma, X. L. Wu, Tailoring heterogeneities in high-entropy alloys to promote strength–ductility synergy. *Nat. Commun.* **10**, 5623 (2019).

42. E. Welsch *et al.*, Strain hardening by dynamic slip band refinement in a high-Mn lightweight steel. *Acta Mater.* **116**, 188−199 (2016).

43. T. Yang *et al.*, Multicomponent intermetallic nanoparticles and superb mechanical behaviors of complex alloys. *Science* **362**, 933−937 (2018).

44. J. D. Yoo, K. T. Park, Microband-induced plasticity in a high Mn–Al–C light steel. *Mater. Sci. Eng. A* **496**, 417−424 (2008).

45. P. J. Shi *et al.*, Multistage work hardening assisted by multi-type twinning in ultrafine-grained heterostructural eutectic high-entropy alloys. *Mater. Today* **41**, 62–71 (2020).
46. S. Cheng *et al.*, An assessment of the contributing factors to the superior properties of a nanostructured steel using in situ high-energy X-ray diffraction. *Acta Mater.* **58**, 2419−2429 (2010).
47. L. L. Ma *et al.*, Reversible deformation-induced martensitic transformation in $Al_{0.6}CoCrFeNi$ high-entropy alloy investigated by in situ synchrotron-based high-energy X-ray diffraction. *Acta Mater.* **128**, 12−21 (2017).
48. Y. J. Shi *et al.*, In situ neutron diffraction study of a new type of stress-induced confined martensitic transformation in $Fe_{22}Co_{20}Ni_{19}Cr_{20}Mn_{12}Al_7$ high-entropy alloys. *Mater. Sci. Eng. A* **771**, 138555 (2020).
49. T. Yang *et al.*, Ultrahigh-strength and ductile superlattice alloys with nanoscale disordered interfaces. *Science* **369**, 427−432 (2020).
50. U. G. K. Wegst *et al.*, Bioinspired structural materials. *Nat. Mater* **14**, 23−36 (2015).
51. G. E. Fantner *et al.*, Sacrificial bonds and hidden length dissipate energy as mineralized fibrils separate during bone fracture. *Nat. Mater* **4**, 612−616 (2005).
52. S. Weiner *et al.*, Rotated plywood structure of primary lamellar bone in the rat: orientations of the collagen fibril arrays. *Bone* **20**, 509−514 (1997).

Acknowledgements The authors recognize G. Liu, P.M. Cheng and P. Zhang at Xi'an Jiaotong University for their help with fracture toughness and nano-indentation tests. The authors also appreciate discussions with Y.Z. Chen of Northwestern Polytechnical University, J.F. Li of Shanghai Jiaotong University and X.H. Xiao of Brookhaven National Laboratory. **Funding:** Y.B.Z. is grateful for financial support from the National Key Research and Development Program of China (2018YFF0109404, 2016YFB0300401, 2016YFB0301401), the National Natural Science Foundation of China (U1732276, U1860202). Y.D.W. is grateful for financial supports from National Science Foundation of China (NSFC) (Grant number 51831003) and the Funds for Creative Research Groups of China (No. 51921001). T.X.Z. is grateful for financial support from the National Natural Science Foundation of China (Grant No. 51704193). Z.S. is grateful for financial support from the National Natural Science Foundation of China (Grant No. 51904184). Use of the Advanced Photon Source was supported by the U.S. Department of Energy, Office of Science, Office of Basic Energy Science, under Contract No. DE-AC02-06CH11357. **Author contributions:** Y.B.Z. and P.J.S. designed the study. P.J.S. carried out the main experiments. D.R., Y.D.W., Y.B.Z., Y.R., W.L.R., Y.Z, P.K.L, R.G.L. and P.J.S. analyzed the data and wrote the main draft of the paper. J.C.P., N.M. and P.F.H. conducted the TEM, LAADF-STEM and HAADF-STEM characterizations. R.G.L. and Y.R. conducted the high-energy synchrotron XRD. X.L. prepared the TEM specimens with a dual-beam FIB. Y.L., Y.B.W, Z.S. and T.X.Z. processed the alloy and tensile samples. All authors contributed to the discussion of the results, and commented on the manuscript. **Competing interests:** The authors declare

no competing interests. **Data and materials availability:** All data are reported in the main paper and supplementary materials.

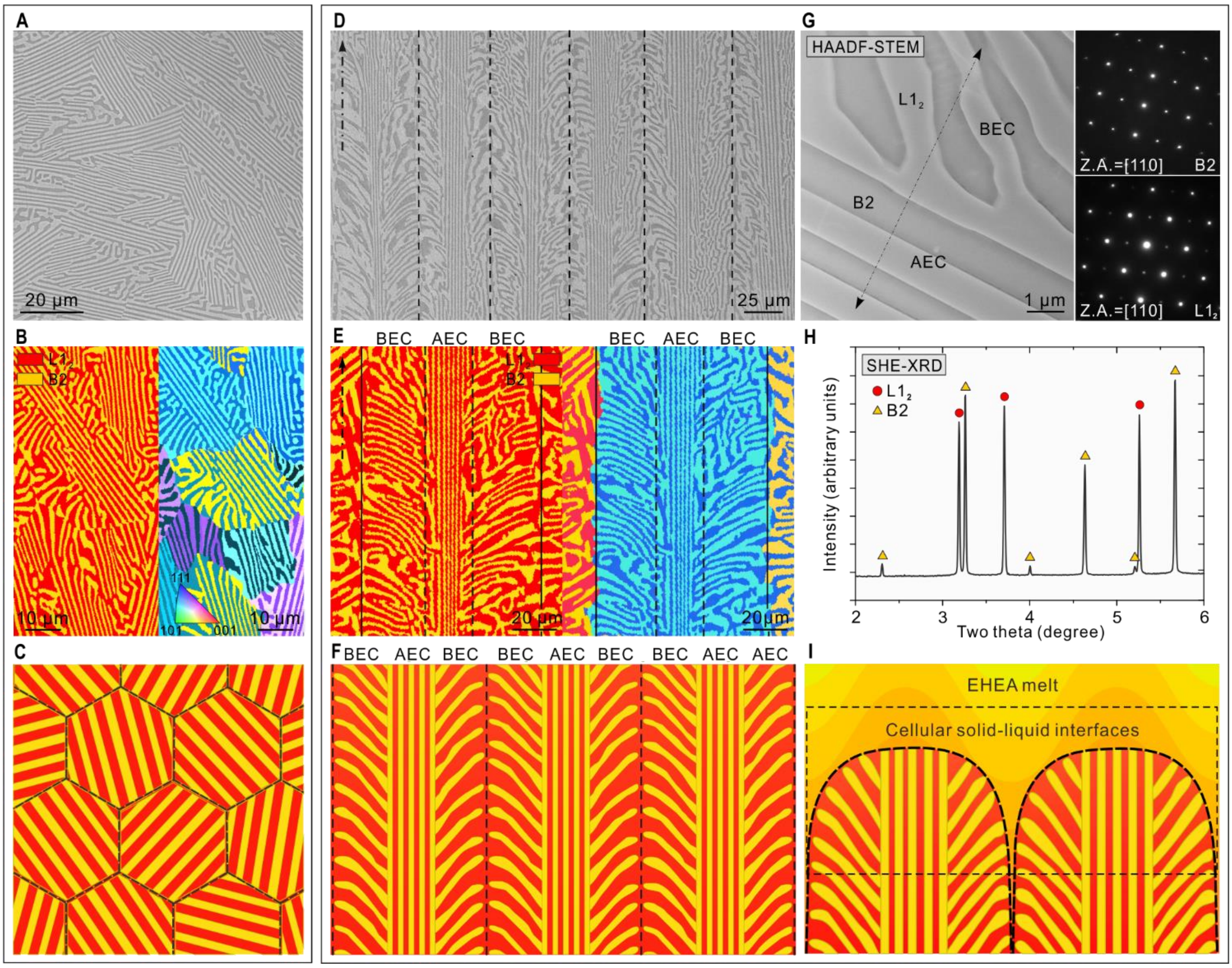

Fig. 1. Hierarchically-arranged herringbone microstructure. (**A** to **C**) Conventionally-cast EHEA serving here as reference material. (**A**) Scanning-electron microscopy (SEM) backscattered electron image. (**B**) Electron back-scattering diffraction (EBSD) phase map (left) and inverse-pole-figure (IPF) map (right). (**C**) Schematic diagram. (**D** to **I**) The directionally-solidified EHEA with a hierarchical herringbone microstructure. The black arrows in (**D**) and (**E**) indicate the DS direction, and also the tensile loading direction in Fig. 2A. (**D**) SEM backscatter electron image showing that the microstructure is composed of columnar grains. Grain boundaries are marked by black dotted lines. **(E)** Enlarged EBSD phase and IPF maps showing the

columnar grain consisting of AEC and BEC. Black solid and dotted lines mark grain and colony boundaries, respectively. (**F** and **I**) Schematic diagram of herringbone structure and its formation principle, respectively. (**G**) HAADF-STEM image and related selected-area electron diffraction patterns of B2 and $L1_2$ phases. The HAADF-STEM image shows clean dual-phase lamellae without evidence of nanoprecipitates or other phases, which is also indicated in (**F**). (**F**) SHE-XRD of B2 and $L1_2$ phases.

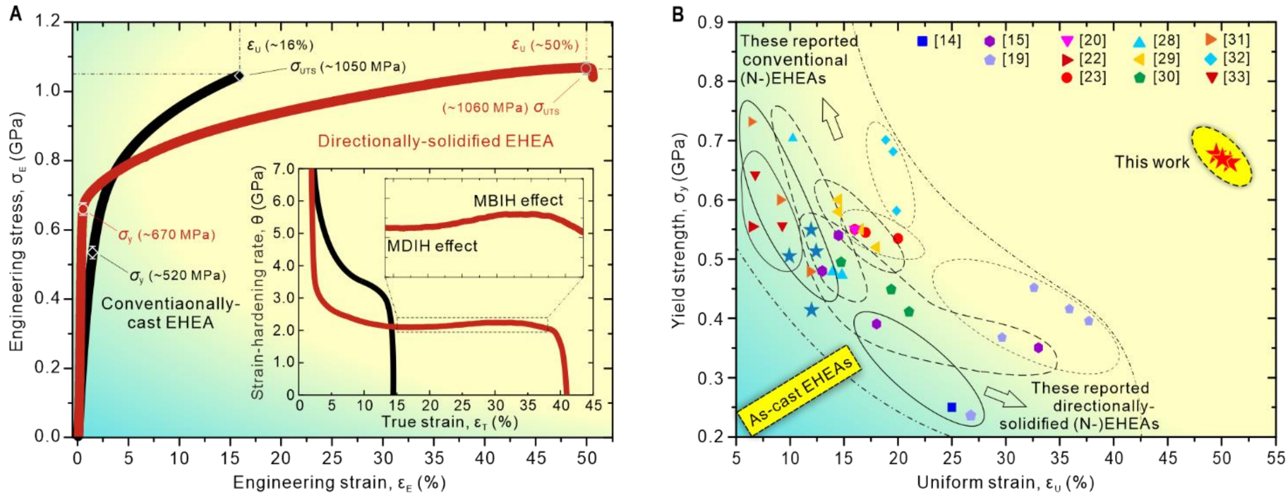

Fig. 2. Tensile response at ambient temperature. (**A**) Engineering stress–strain curves of the directionally-solidified EHEA compared with the conventionally-cast EHEA, displaying a substantial increase in uniform tensile ductility without any strength reduction. The directionally-solidified EHEA shows no post-uniform ductility, which is also confirmed by the absence of macroscopic necking at the fracture end in the inset of fig. S5A. Tensile loading was performed along the DS direction. Inset, the corresponding strain-hardening curves. MDIH and MBIH refer to multi-slip dislocation-induced hardening and microband-induced hardening, respectively. (ε_U) uniform strain. (σ_y) yield strength. (σ_{UTS}) ultimate tensile strength. (**B**) Yield strength versus uniform strain of the directionally-solidified EHEAs compared with those of previously reported as-cast eutectic and near-eutectic HEAs *(14, 15, 19, 20, 22, 23, 28–33)*. These blue pentagrams indicate some of our recently-designed eutectic and near-eutectic HEAs (unpublished). (N-)EHEAs refers to eutectic and near-eutectic HEAs. The conventional (N-)EHEAs include the directly-cast and the arc-melting eutectic and near-eutectic HEAs.

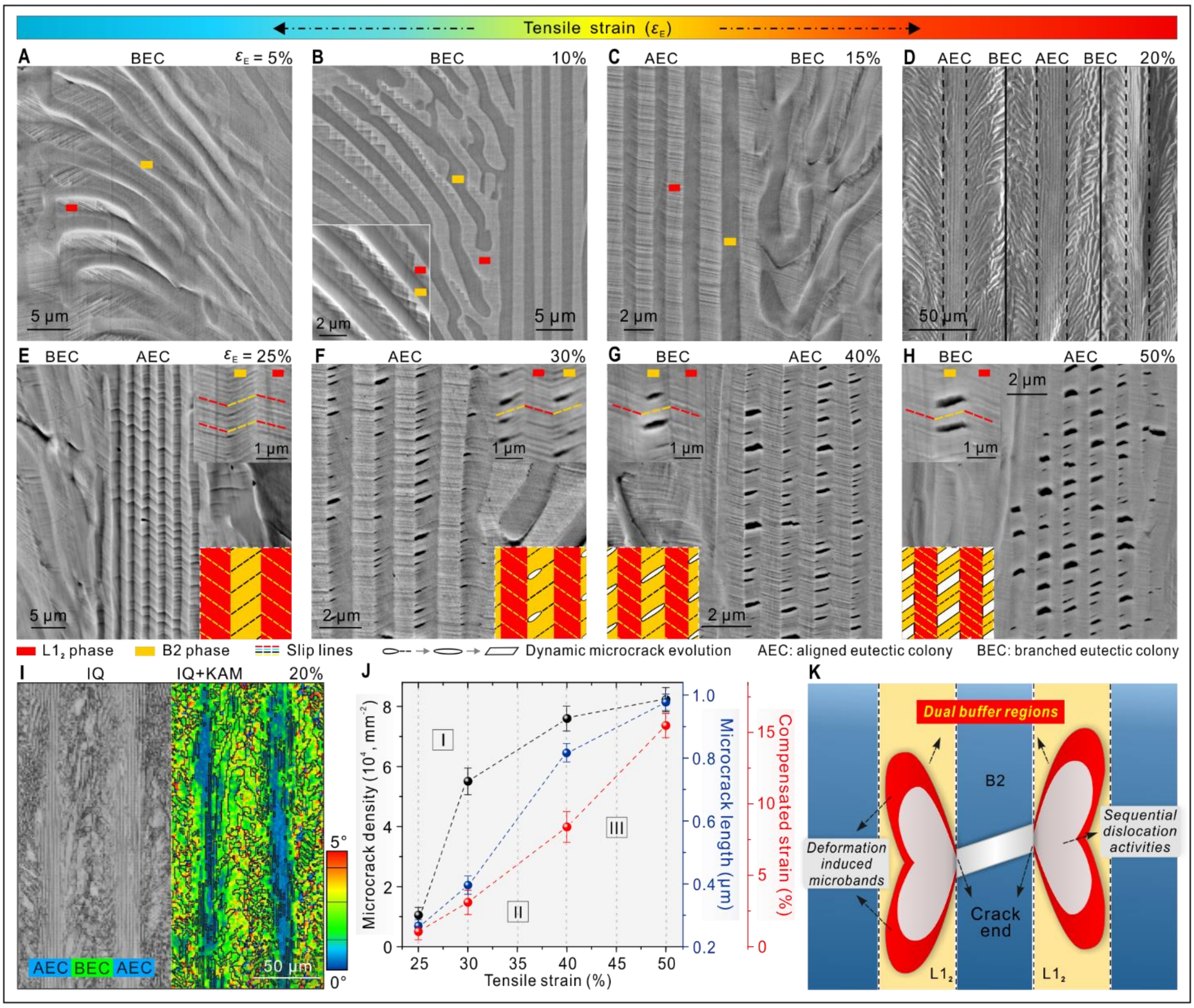

Fig. 3. Hierarchical crack buffering. (**A** to **C**) SEM backscattered electron images showing sequentially-activated slip lines from soft BEC to strong AEC. The inset in (B) shows enlarged cross-slip lines. (**D**) SEM image exhibiting the compatible deformation between adjacent columnar grains and no grain-boundary cracks. Black solid and dotted lines mark grain and colony boundaries, respectively. (**E** to **H**) Well-controlled micro-crack evolution in the AEC. These (upper) enlarged and (lower) colored insets illustrate dynamic micro-crack evolution. (**I**) EBSD-based image quality (IQ) and IQ with kernel average misorientation (KAM) maps. The KAM is calculated up to the fifth neighbour shell with a maximum misorientation angle of 5°, which is indicative of the deformation

degree. (**J**) The evolution of micro-crack length, micro-crack density, and compensated strain in the AEC. Stages I–III correspond to tensile strains of 25–30%, 30%–40%, and 40%–50%. The error bars are standard deviations of the mean. (**K**) Schematic diagram.

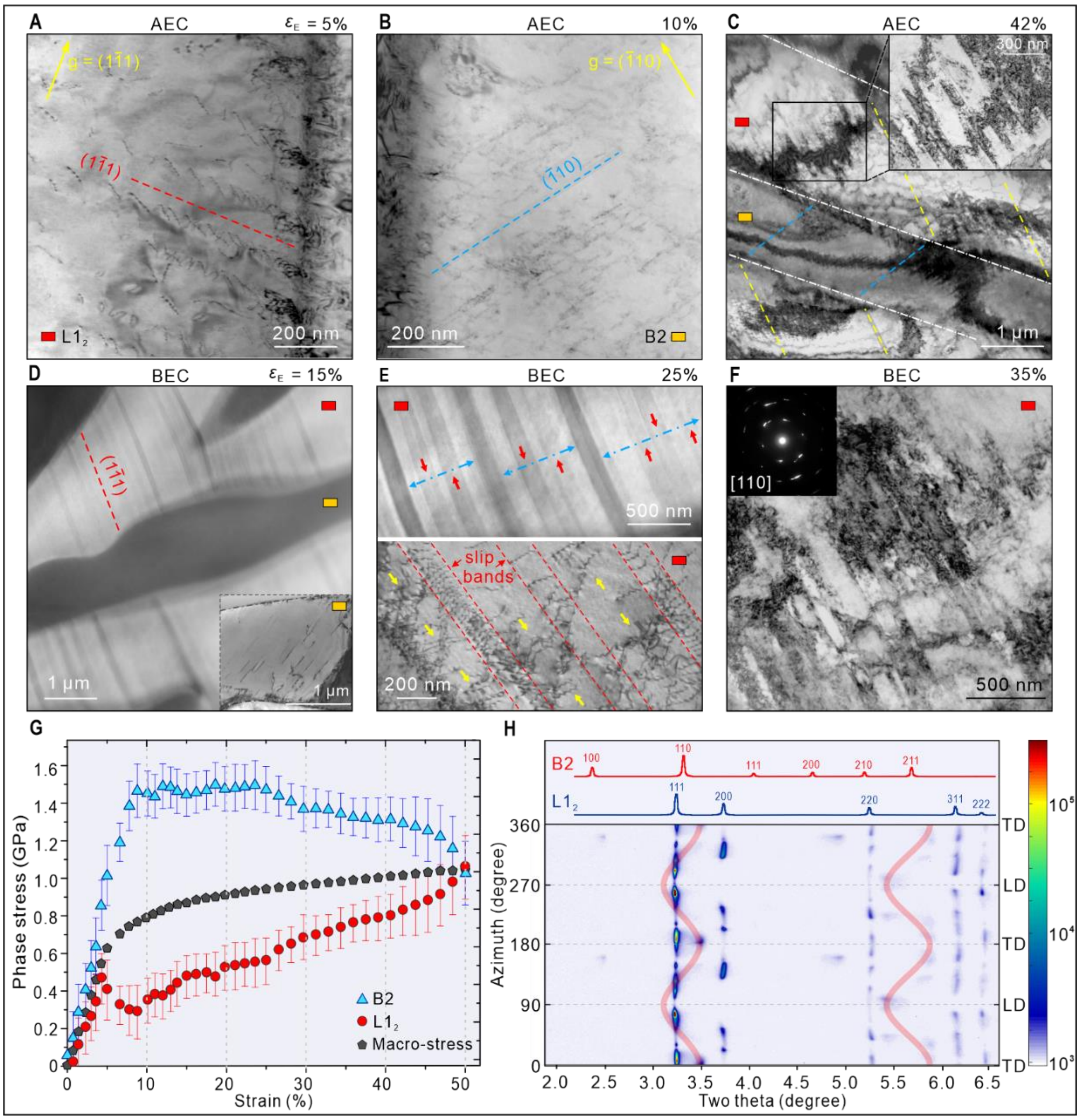

Fig. 4. Microstructural and micromechanical observations of load bearing response for L1$_2$ lamellae. (**A** and **B**) Planar-slip dislocations in L1$_2$ and B2 lamellae, respectively. (**C**) Deformation-induced microbands in L1$_2$ lamellae. The inset exhibits clearer microband structure. (**D** and **E**) Dynamic slip band refinement (D and Upper E shown by HAADF-STEM) and fresh slip bands and cross-slip dislocations marked by red lines and yellow arrows, respectively (Under E). (**F**) Deformation-induced microbands. The ring-like selected-area electron diffraction pattern (inset) suggests that these microbands are similar to low-angle grain boundaries (rather than mechanical twins). The beam directions are [011] in (A, D and E) and [001] in (B). ***g*** indicates the

direction of the diffraction vector. (ε_E) tensile strain. (**G**) Real-time stress partitioning of B2 and $L1_2$ phases (i.e., σ_{B2} and σ_{L12}) during tensile loading (*21*). (**H**) Selected 2D X-ray diffraction images along the full azimuthal angle η (0°–360°) at tensile strain of ~48%. Note that 90° and 180° correspond to the loading direction (LD) and transverse direction (TD), respectively.